

<https://doi.org/10.1038/s41612-024-00826-8>

Distinct tropospheric anomalies during sudden stratospheric warming events accompanied by strong and weak Ural Ridge

Chongyang Zhang¹, Jiankai Zhang¹ ✉, Amanda C. Maycock² & Wenshou Tian¹

Different tropospheric precursor anomalies leading to sudden stratospheric warmings (SSWs) may result in different circulation evolution. This study finds that there are distinct differences in tropospheric circulation evolutions during SSWs following anomalously strong- (SUR-SSWs) and weak- (WUR-SSWs) Ural ridge. SUR-SSWs exhibit enhanced East Asian trough in the following week, while enhanced Greenland ridge and negative tropospheric annular mode anomalies can persist for 1 month. In contrast, WUR-SSWs exhibit surface cooling over northern Eurasia without notable tropospheric annular mode anomalies. During SUR-SSWs, waves induced by the enhanced Ural wave source tend to propagate below the tropopause, amplifying the East Asian trough. Additionally, due to decreased wave phase speed, the preexisting Ural ridge anomalies migrate westward and amplify the Greenland ridge. Before WUR-SSWs, preexisting cooling over Northeast Asia migrates westward and amplifies northern Eurasia cooling. Thus, the Ural ridge anomalies prior to SSWs significantly influence post-SSW tropospheric circulation.

The Arctic stratospheric polar vortex, a strong cyclonic circulation extending from 10 to 50 km above the surface, forms in autumn as the polar night begins. On some occasions, large-scale waves propagating into the stratosphere with persistent and strong eddy heat transport break down the polar vortex and lead to a rapid warming and reversal of westerlies within a few days, a phenomenon known as sudden stratospheric warming (SSW). Planetary wave breaking in the upper stratosphere during SSWs reduces westerlies and extends down the critical layer (the region where the background westerly equals to the zonal phase speed), which is unfavorable for wave propagation. Consequently, waves break at progressively lower altitudes, and the easterly anomalies extend downward into the lower stratosphere^{1,2}. Subsequently, zonal wind and geopotential height anomalies extend downward into the troposphere and even to the surface, giving rise to persistent surface weather anomalies across the Northern Hemisphere in the subsequent weeks or even months, such as extreme cold air outbreaks over northern Eurasia and western Europe³, as well as significant warming over Greenland and eastern Canada^{4,5}. Various mechanisms to explain the downward impact of SSWs have been identified⁶. Geostrophic adjustment to stratospheric potential vorticity (PV) anomalies^{7–15} and transient eddy feedback^{16,17} during SSWs can directly diminish tropospheric westerlies and

promote the negative phase of the Arctic Oscillation (AO). Observations also reveal that waves below the critical layer tend to be reflected during SSWs, leading to local tropospheric circulation anomalies^{18–23}.

While SSWs can yield statistically significant surface anomalies and have been regarded as a crucial source of subseasonal predictability in surface weather^{24–26}, the influence of individual SSW event exhibits considerable variability^{20,27,28,29}, and nearly half of SSWs are not followed by downward propagating signals^{30,31}. Several physical factors have been linked to the likelihood of downward influence of SSWs^{30,32,33}. SSWs following tropospheric negative annular mode anomalies exert a more pronounced downward impact^{6,34} and SSWs preceded by larger tropospheric wave activity may exhibit a stronger tropospheric response³⁵, though some studies suggest no significant difference in vertical wave flux between propagating and non-propagating SSWs³⁶. SSWs featuring stronger and more persistent anomalies in the lower stratosphere could also give rise to more robust surface responses^{11,27,30,36}. A stronger meridional PV gradient in the upper stratosphere preceding SSWs can amplify the surface response³². Wave-absorbing SSWs could induce surface AO anomalies, while wave-reflecting SSWs tend to promote local blocking events²⁰. SSWs characterized by different geometry of the stratospheric polar vortex (vortex displacement and

¹College of Atmospheric Sciences, Lanzhou University, Lanzhou, China. ²School of Earth and Environment, University of Leeds, Leeds, UK.

✉ e-mail: jkzhang@lzu.edu.cn

vortex splitting types, wavenumber 1 and wavenumber 2 types) may yield disparate surface responses³⁷, but some studies found no significant difference in the annular mode response²⁷. It was also suggested that the surface response to splitting types occurs earlier than that for displacement types by 1 week, together with northern Eurasia cooling^{5,38–40}. In addition, some studies suggested that the cooling over East Asia during SSWs is contributed by upstream Ural blockings rather than downward propagating of stratospheric signals^{3,40,41}. Therefore, while the two-way interaction between planetary waves and mean flows contributes to the downward propagation of SSWs, the underlying mechanisms through which surface weather response to SSWs remain incompletely understood^{6,24}.

Anomalous wave sources, such as a ridge and warming over the Ural and Barents-Kara Seas (BKS) region and Aleutian Low^{42–45}, typically serve as the precursors to SSWs⁴⁶; however, whether SSWs preceded by different wave sources exhibit distinct evolutions remains unclear. From the climatological perspective, the strongest wave source triggering upward wave propagation into the stratosphere is situated over the Ural region during winter⁴⁷. Thus, this study examines the dynamical evolution of SSWs following strong (SUR-SSWs) and weak (WUR-SSWs) Ural ridge, corresponding to strong and weak Ural wave sources, respectively. The mechanisms responsible for the distinct circulation evolution in these two types of SSWs are further revealed. The paper is organized as follows: Section 2 introduces the data and methods, while Section 3 outlines our results, which are further discussed in Section 4.

Results

Tropospheric circulation anomalies associated with SUR-SSWs and WUR-SSWs

Figure 1 presents the circulation evolution during SUR-SSWs. Approximately 14 days prior to the onset of SUR-SSWs, sustained warming and positive geopotential height anomalies are observed over the Ural region. A significantly enhanced wave train propagates vertically from the Ural region, inducing anomalous stratospheric wavenumber 1 (Fig. 1c). The wavenumber 1 amplitude in the upper stratosphere is persistently enlarged and ultimately leads to wave breaking from day -7 to day -1, leading to positive geopotential height anomalies in the zonal mean and a weakened stratospheric polar vortex (Fig. 1f). Meanwhile, there remains a wave structure in the lower stratosphere, characterized by positive geopotential height anomalies over the Ural region and negative geopotential height anomalies to the east. From day 0 to day 6 (Fig. 1i), the preexisting wave patterns in the stratosphere dissipate entirely.

In the troposphere, there is enhanced downstream propagation of waves from the Ural region, leading to a strengthening of the East Asian trough and near-surface cooling, which peaks in the week prior to the SSW onset (Fig. 1d, e) and persists during the first week following the SSW (Fig. 1g, h). Additionally, the positive geopotential height anomalies over the Ural region prior to the SSW onset extend westward to the Greenland region. Consequently, the enhanced Ural ridge leads to anomalous atmospheric circulation both downstream and upstream following SUR-SSWs. As will be shown later, the stratospheric state associated with SSW significantly impacts the linkage between the Ural ridge and atmospheric circulation in both directions.

By contrast, ~14 days before the WUR-SSWs, significant negative geopotential height and temperature anomalies emerge over northeastern Asia (around 90°–180°E, 55°–75°N) (Fig. 2a, b). During the week prior to the SSW onset, these negative anomalies extend westward to the Ural region and reach a maximum. Lehtonen et al.³⁸ also suggested that cold anomalies over Northern Eurasia tend to be stronger and more widespread before SSWs onset than after SSWs onset. Therefore, the cooling in Northern Eurasia is closely associated with the westward migration of preexisting cold anomalies. Additionally, from day -7 to day 6 (Fig. 2d–h), positive geopotential height and temperature anomalies appear south of 50°N, particularly over East Asia, contrasting sharply with the anomalies observed during the same period for SUR-SSWs (Fig. 1g, h). Thus, the positions of temperature and geopotential height anomalies

following SSWs depend on the characteristics of preexisting Ural ridge anomalies.

The tropospheric circulation anomalies in the month following the two types of SSW are also distinct (Fig. 3). For SUR-SSWs, persistent positive geopotential height anomalies dominate over the polar troposphere. Notably, there are two peaks of positive geopotential height anomalies: one located over the pole and the other one over the Greenland around 60°N. South of the positive anomalies over the Greenland, negative geopotential height anomalies are observed, forming a dipole pattern resembling the negative phase of the North Atlantic Oscillation (NAO). On the other hand, for WUR-SSWs, the negative geopotential height anomalies over the Ural region dissipate quickly, and no NAO anomaly emerges.

The contrasting circulation evolution during both types of SSWs is reproduced by the CMIP6 multi-model results (Fig. 4). Two weeks prior to the onset of SUR-SSWs, there are significantly positive geopotential height and warm anomalies over the Ural region (Fig. 4a and g). The anomalously strong ridge over Ural region extends westward over time and is located over the Greenland around the SUR-SSWs onset date (Fig. 4c). Additionally, there is persistent cooling and an enhanced trough over East Asia from day -14 to day 6. In contrast, from day -7 to day 6 of WUR-SSWs, there are distinct negative geopotential height and cooling anomalies over the northern and northeastern Eurasia (Fig. 4e, f, k and l), coinciding with a weakened East Asia trough and persistent warming.

To test the sensitivity of the results to the zero-gpm threshold for 500 hPa geopotential height anomalies over the Ural region in the classification of SUR-SSWs and WUR-SSWs (see Methods), we composite circulation anomalies based on the five SUR-SSWs with the strongest Ural ridge and the five WUR-SSWs with the weakest Ural ridge prior to the SSWs for each model. The results are similar to those shown in Fig. 4 (Fig. S1), suggesting that the differences between SUR-SSWs and WUR-SSWs are not strongly dependent on the threshold used in distinguishing SUR-SSWs and WUR-SSWs.

Figure S2 shows the differences in 500 hPa geopotential height after SSW onset derived from the WACCM sensitivity experiments (see Methods). Compared to the CLIMnudge runs, both SUR-SSWs and WUR-SSWs runs exhibit persistent positive geopotential height anomalies over the polar region, particularly in the Atlantic sector. Additionally, the East Asian trough is significantly enhanced during the first week following SUR-SSWs (Fig. S2a), a feature that is not observed in the WUR-SSWs during the same time interval (Fig. S2d). Moreover, a stronger Greenland ridge and East Asia trough are evident in the first week following SUR-SSWs onset compared to WUR-SSWs onset (Fig. S2g). The enhanced Greenland ridge anomalies can persist for up to 20 days after SSW onset (Fig. S2h). Since both runs are nudged toward identical stratospheric conditions, the differences in 500 hPa geopotential height anomalies during the free-run periods between the SUR-SSWs and WUR-SSWs runs reflect atmospheric responses to the Ural ridge anomalies that precede SSWs. Therefore, the simulated differences between SUR-SSWs and WUR-SSWs runs can be attributed to the contrasting Ural ridge anomalies preceding the SSWs. It should be mentioned that these experiments do not consider ocean-atmosphere interactions, which may influence the circulation anomalies following SSWs in the real atmosphere.

The evolution of polar cap averaged geopotential height (PCH) further reveals distinct patterns for SUR-SSWs and WUR-SSWs (Fig. 5a, 5b). In the 2 weeks preceding both types of SSWs, there is a downward extension of positive PCH anomalies from the upper stratosphere (1 hPa) to the tropopause (around 200–300 hPa) over time. Additionally, SUR-SSWs exhibit significant positive PCH anomalies in the troposphere ~10 days before onset, which is primarily contributed by positive geopotential height anomalies over the Ural region (Fig. 1). Moreover, there are significant and enduring positive PCH anomalies and negative westerly anomalies (Fig. 5c) extending to the surface during the 1-month period following the SUR-SSWs, consistent with Fig. 3. Conversely, negative tropospheric PCH anomalies are observed around 10 days before the onset of WUR-SSWs, primarily contributed by negative geopotential height anomalies over

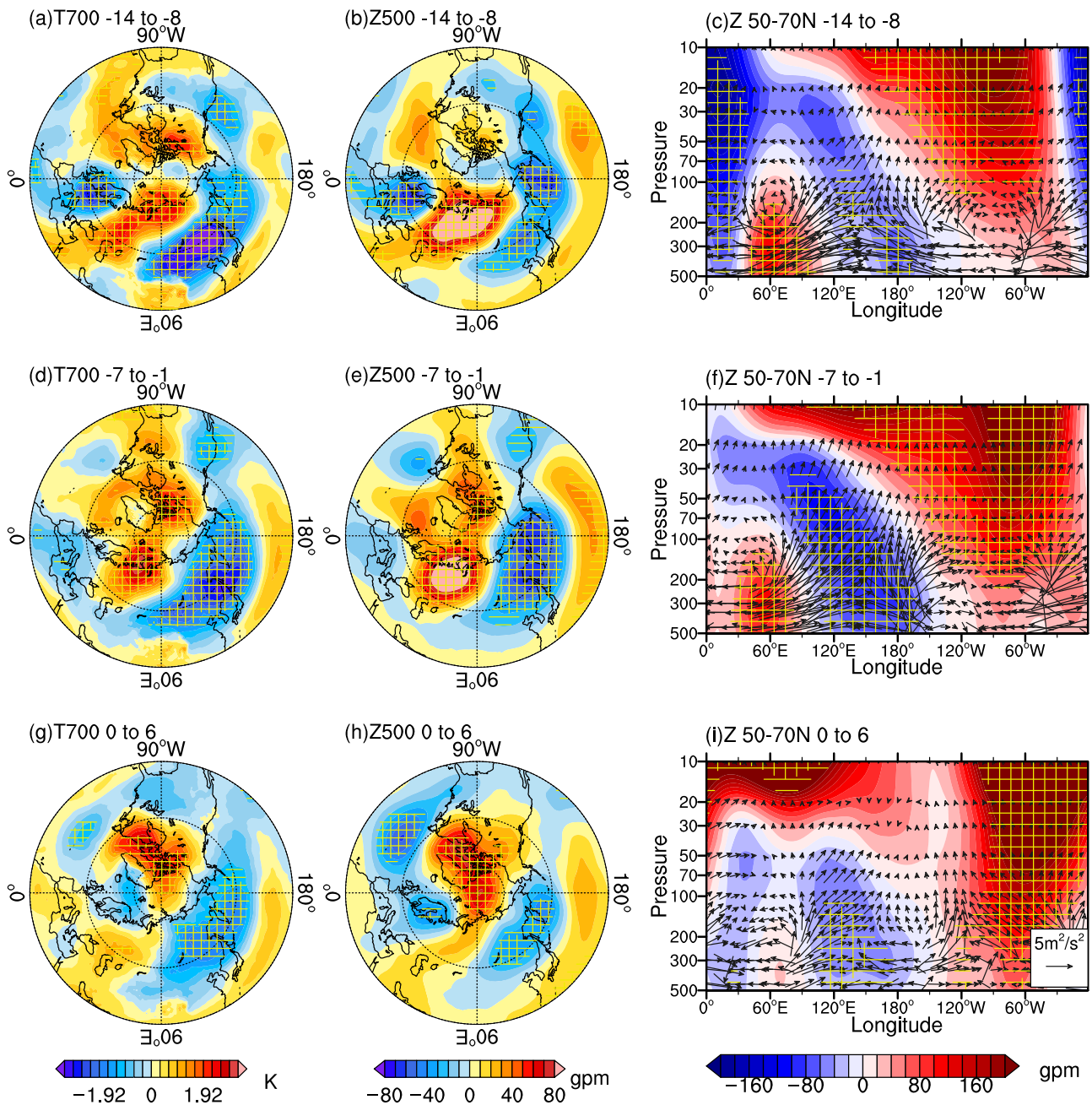


Fig. 1 | Evolution of circulation anomalies from two weeks before to one week after the onset of SUR-SSWs. Composite anomalies in (a) 700-hPa temperature (shading; K), (b) 500-hPa geopotential height (shading; gpm) and (c) geopotential height (shading; gpm) and vertical and meridional components of Plumb wave flux (vectors, m^2/s^2) averaged between 50°N and 70°N from day -14 to day -8 of SUR-

SSWs. The vertical component of vectors is scaled by a factor of 200. **d-f** are the same as (a-c) but from day -7 to day -1 of SUR-SSWs. **g-i** are the same as (a-c) but from day 0 to day 6 of SUR-SSWs. The regions highlighted by vertical (horizontal) parallel lines are statistically significant at the 95% (90%) confidence level according to the Student's *t*-test.

northern Eurasia (Fig. 2). These negative PCH anomalies diminish around the WUR-SSWs onset, with no significant PCH anomalies in the following month (Fig. 5b).

The distinct evolution of PCH during both types of SSW is also evident in the CMIP6 multi-model results (Fig. 4m, n). In these CMIP6 models, stratospheric PCH anomalies during both SUR-SSWs and WUR-SSWs last for at least 40 days on average. However, tropospheric PCH anomalies following SUR-SSWs are significantly stronger than those following WUR-SSWs (Fig. 4o). Despite noticeable zonally asymmetric anomalies in the 500 hPa geopotential height persisting north of 50°N in the week following WUR-SSWs (Fig. 4f), they exhibit a wavenumber-1 pattern rather than yielding a significant zonal mean PCH anomaly.

The modulation of upstream migration of Rossby waves by a weakened stratospheric polar vortex during SSWs

Although the geopotential height anomalies over northern Eurasia prior to SUR-SSWs are opposite to those prior to WUR-SSWs, these anomalies generally exhibit westward migration in both SSW events (Figs. 1 and 2). Figure 6a, b show Hovmöller diagrams of correlation coefficients between 500 hPa geopotential height and 700 hPa temperature over Northeast Asia on day -3 (Fig. 6a), and 500 hPa geopotential height over the Greenland on day 6 (Fig. 6b) of all SSWs, respectively. Notably, the positive correlation centers shift westward over time, indicating the westward migration of waves with a negative zonal phase speed. Consequently, the 700 hPa temperature over Northeast Asia during the 2 weeks prior to SSWs could be

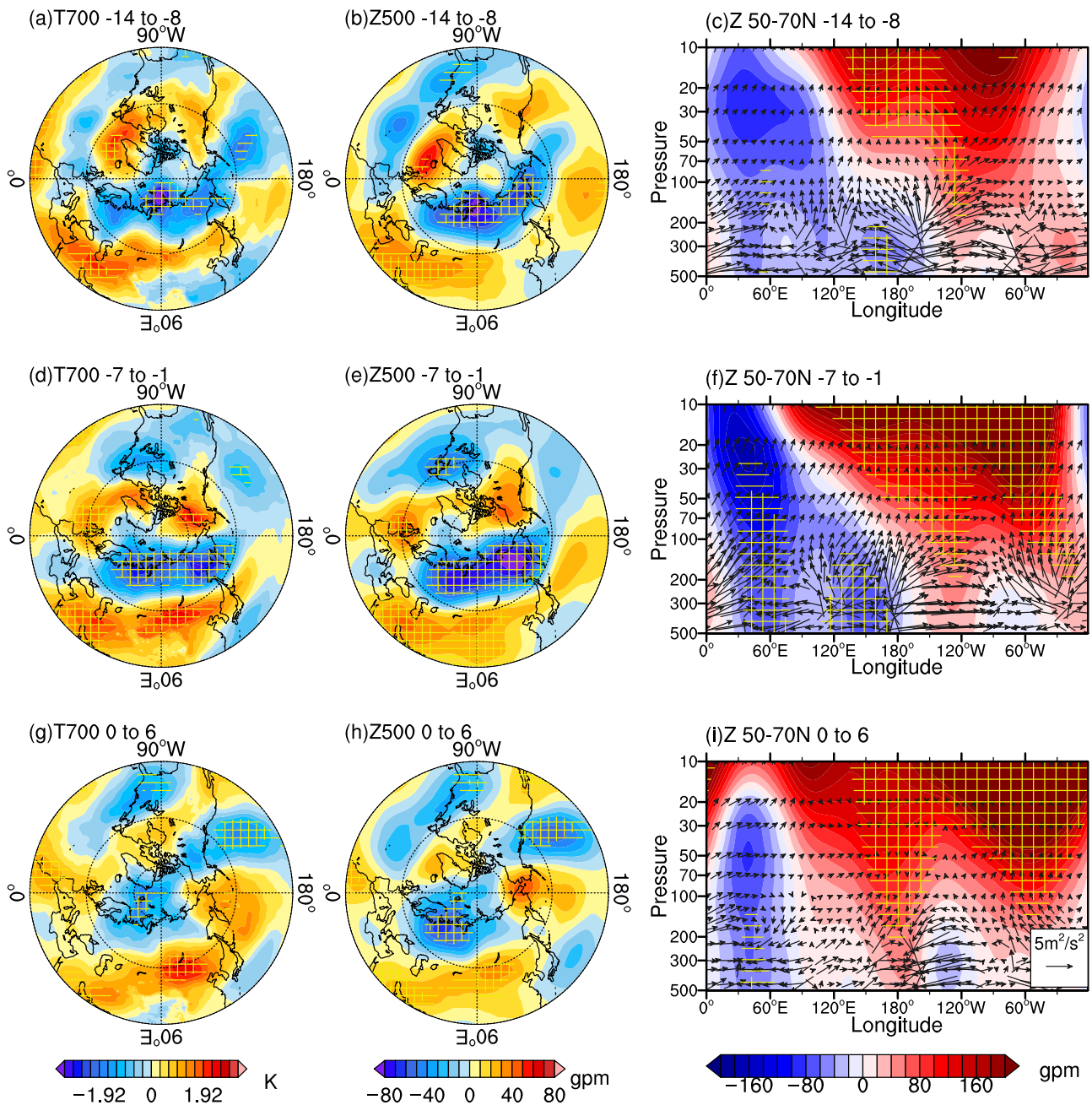


Fig. 2 | Evolution of circulation anomalies from two weeks before to one week after the onset of WUR-SSWs. Composite anomalies in **a** 700-hPa temperature (shading; K), **b** 500-hPa geopotential height (shading; gpm) and **c** geopotential height (shading; gpm) and vertical and meridional components of Plumb wave flux (vectors, m^2/s^2) averaged between 50°N and 70°N from day -14 to day -8 of WUR-

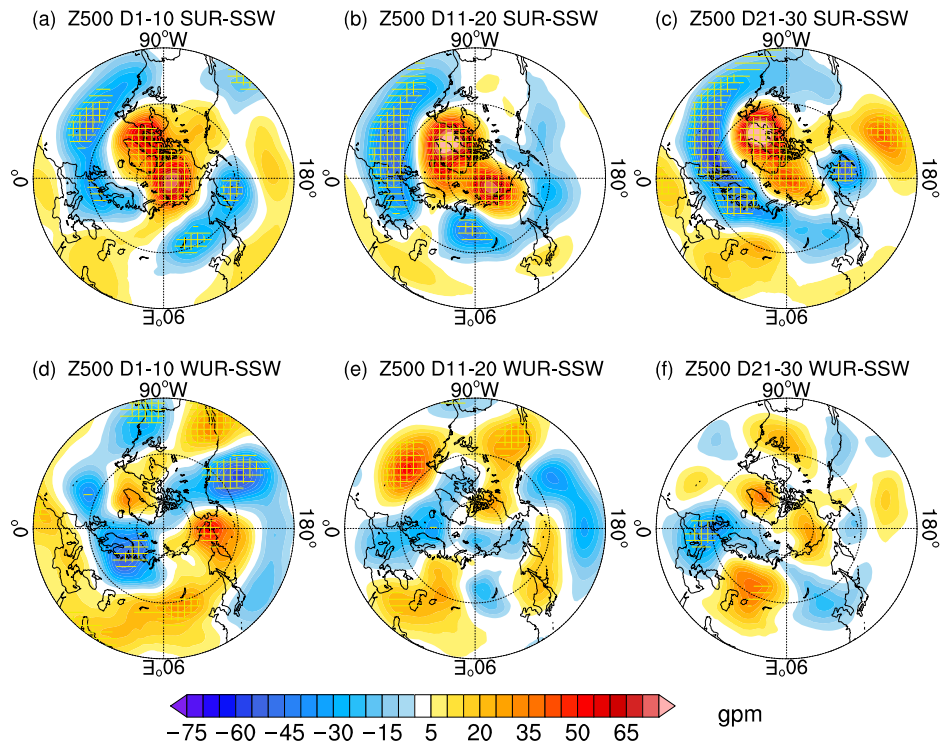
SSWs. The vertical component of vectors is scaled by a factor of 200. **d-f** are the same as (a-c) but from day -7 to day -1 of WUR-SSWs. **g-i** are the same as (a-c) but from day 0 to day 6 of WUR-SSWs. The regions highlighted by vertical (horizontal) parallel lines are statistically significant at the 95% (90%) confidence level according to the Student's *t* test.

used to predict the geopotential height anomalies over northern Eurasia around the SSW onset (Fig. 6a). Likewise, the 500 hPa geopotential height over the Ural region during the 2 weeks prior to SSWs could be used to predict the 500 hPa geopotential height over the Greenland (Fig. 6b). This suggests that the westward migration of positive geopotential height anomalies over the Ural region prior to SUR-SSWs toward the Greenland after SSWs is important for the persistent positive PCH anomalies in the troposphere (Fig. 5a).

Figure 5e, f present the evolution of zonal phase speed for both SUR-SSWs and WUR-SSWs. From day -10 to day 30 of both types of SSW, the phase speed of tropospheric waves is smaller than its climatology, consistent with the findings of Schutte et al.⁴⁸. It has been

demonstrated that weak stratospheric polar vortex can weaken tropospheric westerlies and consequently lead to the westward movement of Ural blockings⁴⁹. Theoretically, weak stratospheric polar vortex can weaken tropospheric westerlies through the rearrangement of stratospheric PV anomalies and transient eddy feedbacks^{16,18,50}. As the phase speed of Rossby waves is proportional to the background westerlies^{51,52}, a reduction in the phase speed of tropospheric waves under weak stratospheric polar vortex conditions is expected. In conclusion, weak stratospheric polar vortex could promote the westward migration of preexistent anomalous high (low) over the Ural (northern Asian) region prior to SUR-SSWs (WUR-SSWs) by reducing tropospheric westerlies and the phase speed of waves.

Fig. 3 | Evolution of tropospheric geopotential height anomalies in the month following the onset of SUR-SSWs and WUR-SSWs. Composite anomalies in 500-hPa geopotential height (shading; gpm) from (a) day 1 to day 10, (b) day 11 to day 20, and (c) day 21 to day 30 of SUR-SSWs. d–f are the same as (a–c) but for WUR-SSWs. The regions highlighted by vertical (horizontal) parallel lines are statistically significant at the 95% (90%) confidence level according to the Student's *t*-test.



The modulation of downstream Rossby wave propagation by a weakened stratospheric polar vortex during SSWs

Although waves propagating from the Ural ridge play a crucial role in the enhanced East Asia trough and cooling associated with SSWs (Fig. 1), the weak stratospheric polar vortex as the large-scale background flow may also modulate wave propagation and thus the linkage between the enhanced Ural ridge and East Asia trough. Before the onset of both types of SSWs, the reduction in negative frequency of refractive index conditions above the tropopause (Fig. 5g and h) favors the upward propagation of tropospheric waves into the stratosphere. Consequently, waves induced by the enhanced Ural wave source are more prone to propagate into the stratosphere during this period. The amplified stratospheric waves subsequently break (Fig. 5i, j) and trigger SSWs. After day -5, there is an increased occurrence of negative refractive index squared conditions above the tropopause, which inhibits upward wave propagation. Previous studies have demonstrated that vertical wave propagation tends to be constrained when the static stability near the tropopause is anomalously high^{53,54}, a feature observed during SSWs⁵⁵. White et al.⁵⁶ applied stratospheric heating perturbations to trigger SSWs, and found that upward wave propagation would be suppressed as a direct response to the SSWs. As a result, waves induced by the enhanced Ural wave source during SUR-SSWs tend to propagate below the tropopause downstream, thereby enhancing the East Asia trough.

The change in vertical wave propagation is further verified by a Hovmöller diagram (Fig. 6c, d). The Ural geopotential height on day -6 is positively correlated with that from day -15 - -6 before the SSW onset (Fig. 6c), alongside the upward propagation of planetary waves between 60° and 180°E (Fig. 6d). However, after day -6, the vertical component of wave flux no longer exhibits sensitivity to the Ural geopotential height on day -6, indicating a suppression of upward wave propagation. Concurrently, the Ural geopotential height on day -6 is negatively correlated with the tropospheric geopotential height downstream (90°-150°E) around day 6, reflecting an eastward propagating wave train confined below the tropopause. Therefore, the geopotential height over the Ural region before the onset of SSWs could serve as a predictor for both upstream and downstream circulation after SSWs.

Another indication of the preferred wave propagation below the tropopause is the increased RWB frequency observed in the month following SSWs (Fig. 5i and j). As waves tend to propagate and amplify below the tropopause, they eventually break, leading to irreversible heat and PV exchange between middle and high latitudes⁵⁷ in the troposphere. The transient eddy feedback as a response to SSW plays an important role in the formation of negative AO anomalies and the reduction of tropospheric westerlies at high latitudes⁵⁸. Notably, increased RWB frequency can be observed following both types of SSWs and is a process relatively independent of the Ural ridge anomalies preceding the SSWs.

Amplification of the significance of Ural ridge anomalies for tropospheric circulation by SSWs

To further understand the significance of SUR-SSWs in tropospheric weather forecasting, we analyzed the relationships between Ural ridge anomalies on day -6 and geopotential height on day 0 and day 6 during SSWs compared to those during SPVs. We also selected all typical winter days characterized by Ural geopotential height anomalies exceeding ± 0.5 standard deviation during winter, examining the relationships between the typical Ural ridge anomalies and geopotential height 6 and 12 days later (Fig. 7).

For SSWs, positive correlations between Ural ridge anomalies on day 6 and 500 hPa geopotential height on day 0 appear as a band extending from the Ural region to the Atlantic sector (Fig. 7a). These positive correlation centers further migrate westward to the Atlantic sector by day 6 (Fig. 7b). Such westward migration of ridge anomalies is absent during SPV events (Fig. 7d, e). Moreover, for SSWs, significant negative correlations between Ural ridge anomalies on day -6 and 500 hPa geopotential height over East Asia persist until day 6 (Fig. 7b), a phenomenon not observed for SPV events (Fig. 7e) and for days with typical Ural ridge anomalies (Fig. 7h). This suggests an intensified linkage between the Ural ridge and the East Asian trough during SSWs, which could be attributed to suppressed vertical wave propagation and therefore enhanced wave propagation from Ural ridge below the tropopause.

Interestingly, for SPV events, the negative correlations between Ural ridge anomalies on day -6 and 500-hPa geopotential height over East Asia

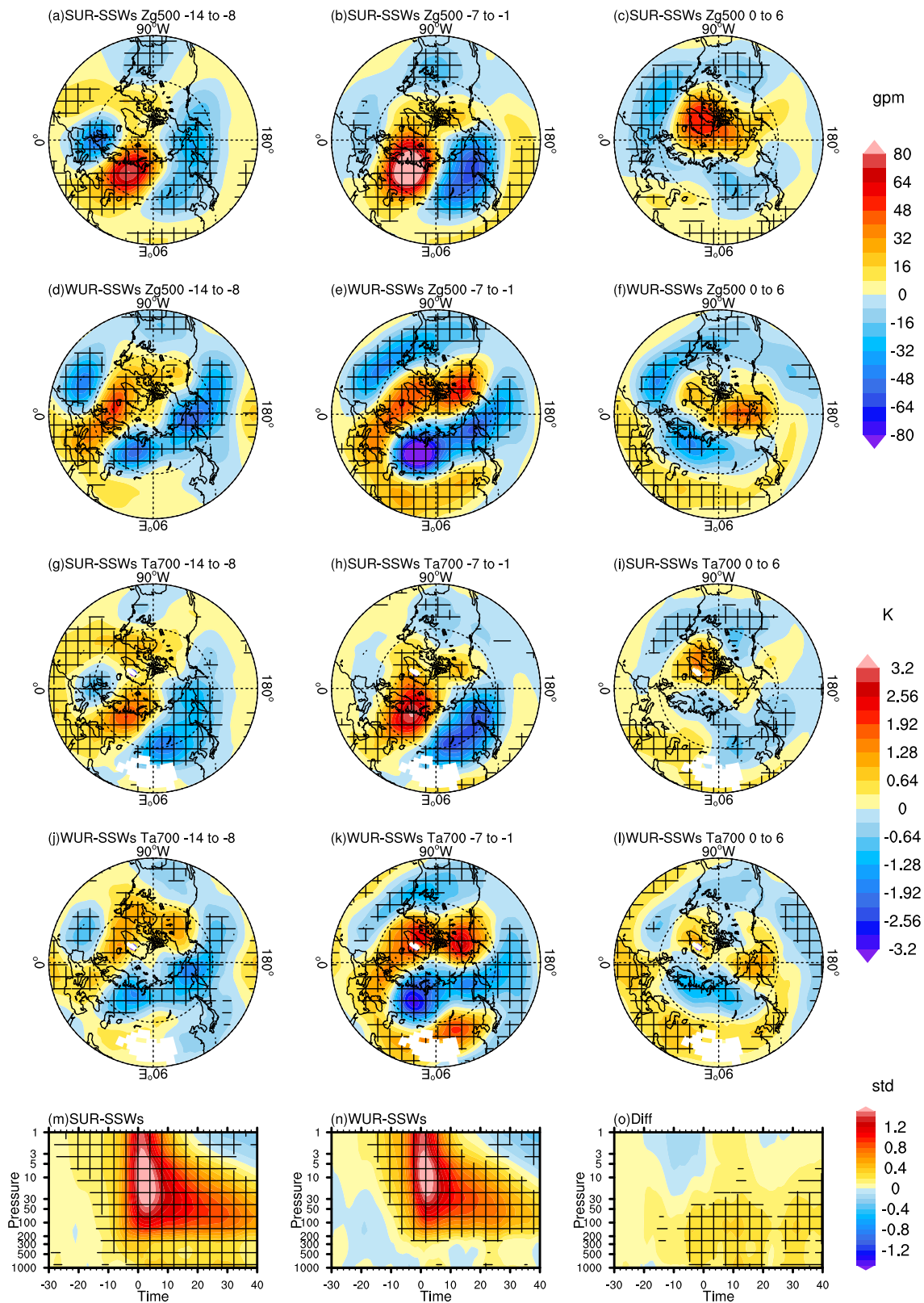


Fig. 4 | Evolution of tropospheric circulation anomalies during SUR-SSWs and WUR-SSWs, derived from CMIP6 models. Composite anomalies in 500-hPa geopotential height (shading; gpm) from (a) day -14 to day -8, (b) day -7 to day -1 and (c) day 0 to day 6 of SUR-SSWs based on CMIP6 multi-model mean results. **d-f** are the same as (a-c), but for the WUR-SSWs, respectively. **g-l** are the same as (a-f), but for the 700 hPa temperature (shading; K). In (g-l), the regions with topographic altitude >3000 m are masked. Time-pressure cross section of composite anomalies in the area

weighted geopotential height north of 60°N normalized by the standard deviation of each pressure level and each CMIP6 models during winter (shading; standard deviation) for (m) SUR-SSWs, (n) WUR-SSWs and (o) their differences. The x-axis denotes the relative day with respect to the onset date of SSW (day 0). The composite anomalies of fields during SUR-SSWs and WUR-SSWs for individual model are used for calculating multi-model mean. The regions highlighted by vertical (horizontal) parallel lines are statistically significant at the 95% (90%) confidence level according to the Student's *t*-test.

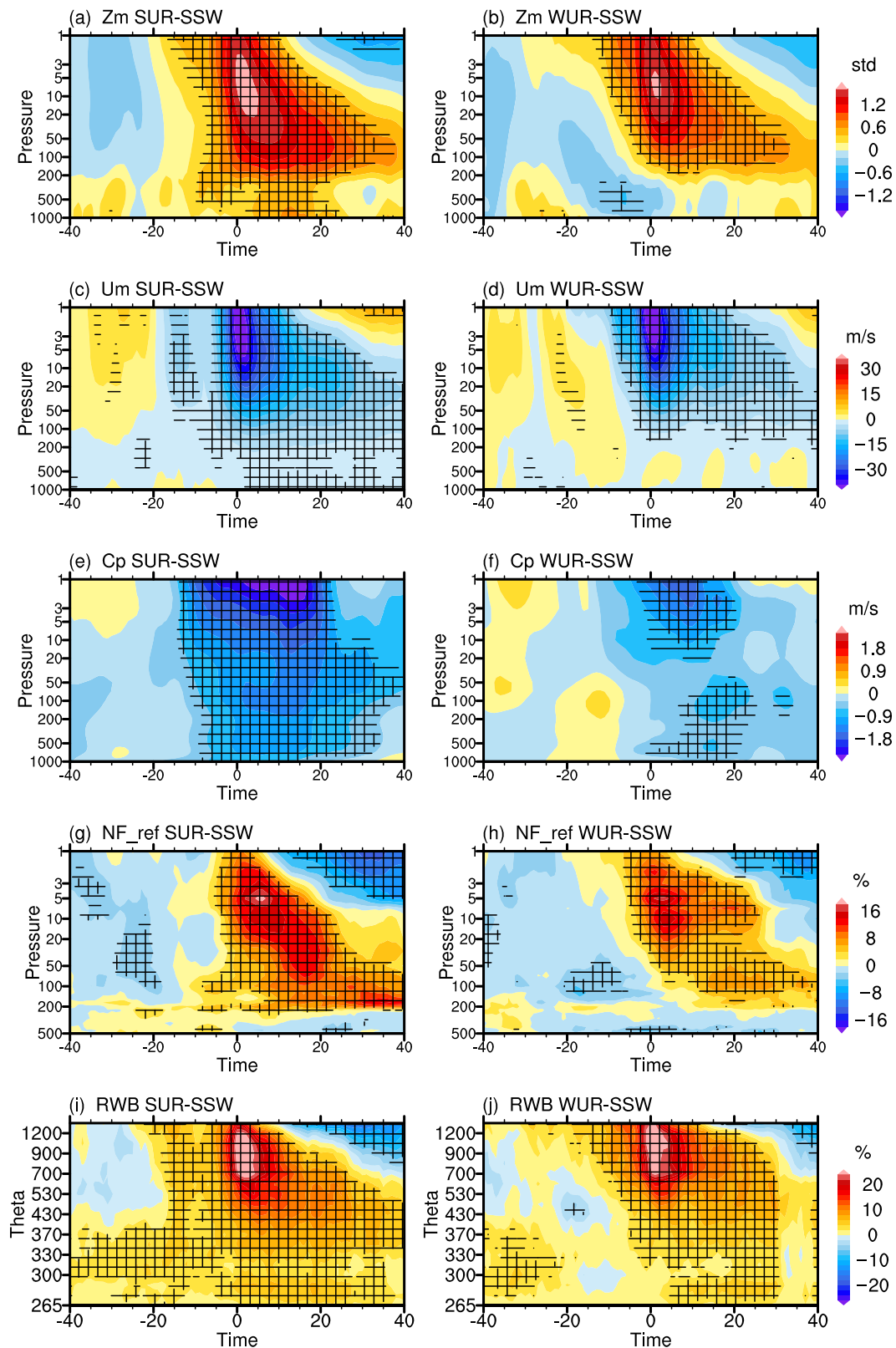
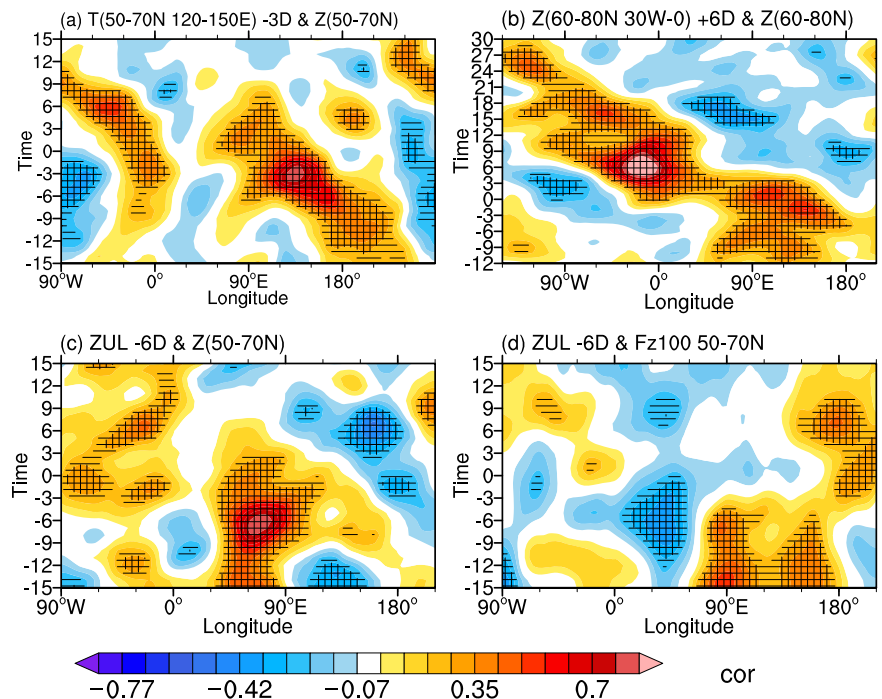


Fig. 5 | Evolution of anomalies in polar cap geopotential height, westerlies, zonal phase speed, negative frequency of the wave refractive index squared, and Rossby wave breaking frequency during SUR-SSWs and WUR-SSWs. Time-pressure cross-section of composite anomalies in the area weighted geopotential height north of 60°N normalized by the standard deviation for each pressure level during winter (shading; standard deviation) for (a) SUR-SSWs and (b) WUR-SSWs, derived from ERA5 reanalysis data. c, d Are the same as (a, b), respectively, but for the area weighted westerlies north of 60°N (shading; m/s). e, f Are the same as (a, b), respectively, but for the

phase speed of Rossby waves in the latitude band of 50–80°N (shading; m/s). g, h Are the same as (a, b), respectively, but for the negative frequency of refractive index squared for wavenumber 1 in the latitude band of 50–80°N (shading; %). i, j are the same as (a, b), respectively, but for the time-potential temperature cross-section of Rossby wave breaking frequency on isentropic surfaces in the latitude band of 50–80°N (shading; %). The x-axis denotes the relative day with respect to the onset of SSW (day 0). The regions highlighted by vertical (horizontal) parallel lines are statistically significant at the 95% (90%) confidence level according to the Student’s *t*-test.

Fig. 6 | Hovmöller diagrams for the lead-lag correlation associated with geopotential height over the Greenland, Northeast Asia, and Ural regions.

a Correlation coefficients between 700-hPa temperature over northeast Asia (120–150°E and 50–70°N) on day –3 and 500-hPa daily geopotential height averaged between 50°N and 70°N around the onset of all SSWs. **b** Correlation coefficients between 500 hPa geopotential height over the Atlantic region (30°W–0°E and 60–80°N) on day 6 and 500 hPa daily geopotential height averaged between 60°N and 80°N. **c** Correlation coefficients between 500-hPa geopotential height over the Ural region (60°N–80°N and 60–80°E) on day –6 and 500 hPa daily geopotential height averaged between 50°N and 70°N. **d** Correlation coefficients between 500 hPa geopotential height over the Ural region on day –6 and 100 hPa vertical component of wave flux averaged between 50°N and 70°N. The y-axis denotes the relative days with respect to the onset of SSW (day 0). The regions highlighted by vertical (horizontal) parallel lines are statistically significant at the 95% (90%) confidence level according to the Student's *t*-test.



on day 0 (Fig. 7d) are weaker than those 6 days following typical Ural ridge anomalies (Fig. 7g). The weaker connection between Ural ridge and the East Asia trough than normal could be explained by decreased negative frequency of refractive index squared under SPV conditions⁵⁰, promoting upward propagation of waves induced by the Ural wave source (Fig. S3b), corresponding to weakened horizontal wave propagation below the tropopause.

Furthermore, for SSWs, the Ural ridge anomalies on day –6 exhibit a significant positive correlation with tropospheric PCH until around day 16 of SSWs (Fig. 7c), consistent with Figs. 3 and 5a. On the other hand, such significant positive correlations almost disappear on day 5 of SPV events (Fig. 7f) and 14 days after typical Ural ridge anomalies (Fig. 7i). For SPVs, significant positive correlations between Ural ridge anomalies on day –6 and tropospheric PCH around day reemerge on day 35 and extend from the upper stratosphere. Again, due to decreased negative frequency of refractive index squared under SPV conditions, waves associated with the enhanced Ural ridge tend to propagate into the stratosphere (Fig. S3b) and imprint anomalous signals there. Overall, SSWs could amplify the importance of Ural ridge anomalies in forecasting circulation patterns over the Atlantic sector, East Asia, and the PCH.

Discussion

In this study, the circulation evolution during WUR-SSWs and SUR-SSWs are found to be fundamentally distinct, as illustrated in Fig. 8. Prior to SUR-SSWs, there is enhanced ridge and prolonged warming over the Ural region. Simultaneously, upward wave propagation from the Ural region is enhanced, leading to the persistent amplifying and breaking of stratospheric waves and weakening the stratospheric polar vortex. The increased occurrence of negative refractive index squared conditions above the tropopause after SSWs is unfavorable for the vertical propagation of waves (Fig. 5g). Consequently, the wave train induced by the enhanced Ural wave source is confined below the tropopause and propagates downstream, enhancing the trough and cooling over East Asia in the first week following SUR-SSWs. Additionally, the weak stratospheric polar vortex conditions decelerate tropospheric westerlies (Fig. 5c) and consequently reduce the phase speed of Rossby waves (Fig. 5e), promoting the westward migration of positive geopotential height anomalies over the Ural region toward the Greenland (Figs. 6b and 7a, b). The persistence of the enhanced Greenland ridge further

contributes to positive anomalies of tropospheric PCH and the negative phase of NAO (Fig. 3a, b) lasting for 1 month following SUR-SSWs (Fig. 3a–c). In contrast, prior to WUR-SSWs, due to the westward migration of negative geopotential height from the northeast Asia, there are negative geopotential height anomalies and cooling over Northeast Asia from day 0 to day 6, accompanied by weakened trough and warming over East Asia (Fig. 2). Additionally, there are no significant PCH anomalies in the month following WUR-SSWs (Fig. 3). Therefore, persistent PCH anomalies in the troposphere during SUR-SSWs are more likely to be observed compared to WUR-SSWs.

Previous studies have suggested that the El Niño Southern Oscillation (ENSO) has profound implications for the occurrence of SSWs^{59–64}. We found that the occurrence probability of SUR-SSWs is higher during La Niña winters than during El Niño winters, and vice versa for WUR-SSWs (Table S3). Luo et al.⁶⁵ found that 500-hPa geopotential height anomalies over the Ural region are higher during La Niña winter than that during El Niño winters. However, similar results can be obtained based on the 20 SUR-SSWs and 8 WUR-SSWs during neutral ENSO conditions, suggesting that our results are not significantly impacted by ENSO (Fig. S4). In addition, the combination of reduced Arctic sea ice and SSWs has been reported to enhance the likelihood of regional extreme weather events following SSWs^{66–68}. Since sea ice anomalies can persist for several months, this could modulate surface anomalies associated with stratospheric disturbances over an extended timescale⁶⁹. Further investigation is needed to disentangle the relative contributions of Arctic sea ice loss to the different types of SSWs.

By comparing the circulation evolution associated with an enhanced Ural ridge prior to SSWs and SPV events, and those following days with typical Ural ridge anomalies, it is found that the aforementioned dynamical processes associated with Ural ridge anomalies prior to SSWs are unique. The Ural ridge anomalies on day –6 SSWs are linearly correlated with enhanced ridge over the Atlantic sector, East Asia trough in the first week after SSWs, and tropospheric PCH until day 16 of SSWs (Fig. 7). This phenomenon is not observed following the Ural ridge anomalies prior to SPV events or typical Ural ridge anomalies. Therefore, the significance of Ural ridge anomalies for extended-range weather prediction in the northern hemisphere is amplified by the stratospheric state associated with SSWs.

Despite significant positive geopotential height anomalies over the polar troposphere from days 17–30 following SUR-SSWs (Figs. 3c and 5a),

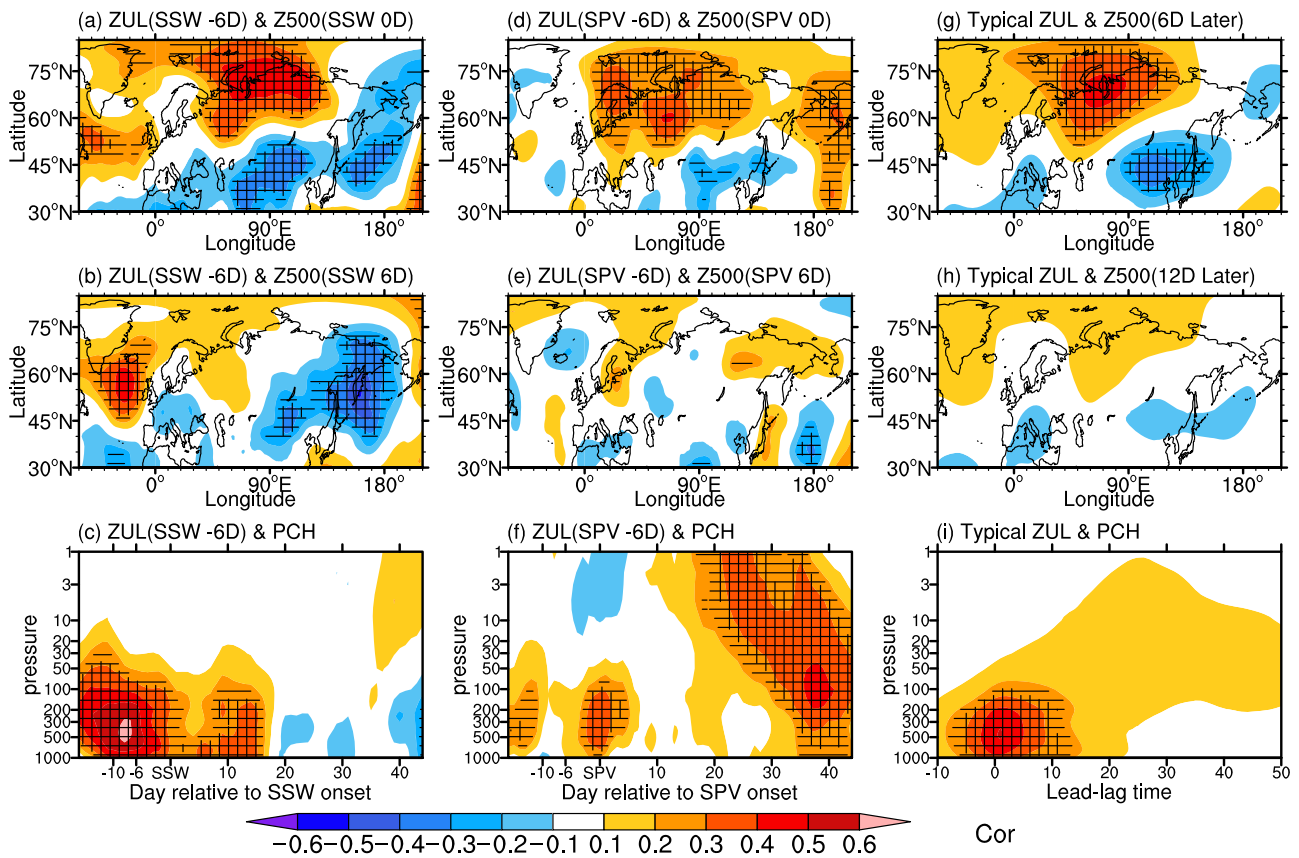


Fig. 7 | Lead-lag correlations associated with geopotential height over the Ural region on day -6 of SUR-SSW, WUR-SSW, or days with typical Ural Ridge anomalies. Lead-lag correlations between 500-hPa geopotential height over the Ural region (60°N–80°N and 60–80°E) on day –6 and 500-hPa geopotential height on (a) day 0 and (b) day 6 of SSWs. c Lead-lag correlations between 500-hPa geopotential height over the Ural region on day –6 of SSWs and PCH. d–f Are the same as (a–c), respectively, but for correlations associated with 500 hPa geopotential height over the Ural region on day –6 of SPVs. g, h Are correlations between 500 hPa geopotential height over the Ural region for all days with a typical Ural ridge anomalies (when the amplitude of the Ural geopotential height anomalies exceeds ± 0.5 standard deviation in December to March) and 500 hPa geopotential height after (g) 6 days and (h) 12 days. i Lead-lag correlations between 500 hPa geopotential height

over the Ural region for all days with a typical Ural ridge anomalies and PCH. The x-axis in (c) and (f) denotes the relative days before and after the onset of SSW (SPV). The x-axis in (i) denotes the lead or lag day, where positive values denote that Ural geopotential height leads PCH. The regions highlighted by vertical (horizontal) parallel lines are statistically significant at the 95% (90%) confidence level according to the Student’s *t*-test in (a–f). In (g–i), significance is determined using the bootstrap method with 1,000 resamples, each with a sample size of 60, to avoid overestimating equivalent degrees of freedom significance is determined using the bootstrap method with 1,000 resamples, each with a sample size of 60, to avoid overestimating equivalent degrees of freedom in the Student’s *t*-test due to auto-correlation of time series.

the Ural ridge anomalies on day -6 are not significantly linearly correlated with PCH during this period (Fig. 7c). Additionally, negative Ural ridge anomalies preceding WUR-SSWs are not followed by significant negative PCH anomalies (Figs. 3d–f and 5b). Due to the increased RWB frequency (Fig. 5i and j) and associated eddy feedback following both types of SSWs, positive tropospheric PCH anomalies can be induced³⁸, thereby amplifying the positive PCH anomalies following SUR-SSWs and masking the negative PCH anomalies associated with negative Ural ridge anomalies for WUR-SSWs. Overall, the enhanced Ural ridge anomalies could contribute to positive tropospheric PCH from day 0 to day 16 following SUR-SSWs through their westward migration toward the Greenland. This positive tropospheric PCH from day 17 to day 30 following SUR-SSWs may be sustained by other factors such as an increased frequency of RWB and associated eddy feedbacks.

Karpechko et al.³⁰ identified a significantly positive correlation between the 150 hPa PCH from day 0 to day 4 of SSW onset and the 1000-hPa PCH from day 8 to day 52 (their Fig. 4), indicating the role of early anomalies in PCH around the tropopause in enhancing extended-range predictability. We found that when the 90 day high-pass filter is applied, the two indices show a slightly negative correlation, indicating that this correlation is primarily contributed by low-frequency variability with periods >90 days (Fig.

S5a, b). It is noteworthy that a similar positive correlation is found when data from all winter days are considered, indicating their broader relevance beyond SSW events (Fig. S5c, d). While our study highlights a distinctive leading correlation between Ural ridge anomalies preceding SSWs and subsequent surface responses in the first 20 days following SSW. This correlation does not exhibit similar characteristics during SPV events or following typical Ural ridge anomalies (Fig. 7), suggesting a different mechanism from Karpechko et al.³⁰ Furthermore, the 150 hPa PCH during days 0–4 and the 1000 hPa PCH during days 8–52 for SUR-SSWs are greater than those for WUR-SSWs, suggesting that the stronger 1000 hPa PCH during days 8–52 for SUR-SSWs is partly contributed by the stronger 150 hPa PCH during days 0–4 (Fig. S5a). After removing the linear component related to 150 hPa PCH during days 0–4, the values of 1000 hPa PCH during days 8–52 (Fig. S5e) and that during days 8–22 (Fig. S5f) for SUR-SSWs remains greater than that for WUR-SSWs, indicating that the Ural high indeed modulates the impacts of SSWs on surface weather.

This study emphasizes the role of Ural ridge anomalies as drivers in shaping anomalous circulation patterns both upstream and downstream, and the role of SSW as a modulator in the propagation and migration of waves associated with the enhanced Ural ridge. Therefore, the evolution of tropospheric circulation associated with SUR-SSWs cannot be explained as

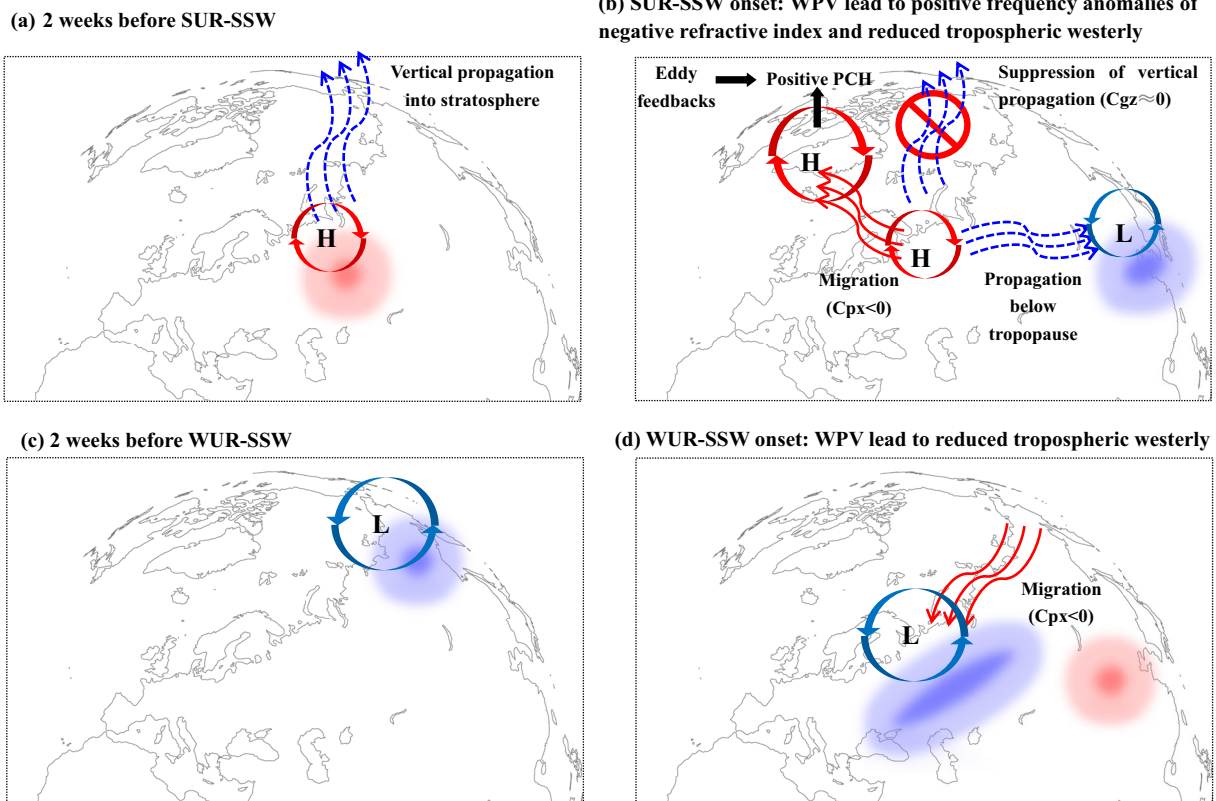


Fig. 8 | Schematic diagram illustrating the evolution of SUR-SSWs and WUR-SSWs. Circulation anomalies (a) two weeks prior to, and (b) around the onset of SUR-SSWs; circulation anomalies (c) two weeks prior to, and (d) around the onset of WUR-SSWs. Cpx and Cgz denote the zonal component of phase speed and vertical

component of group speed of Rossby waves, respectively. The red and blue arrows denote the migration and propagation of waves. The red and blue cycles denote anticyclonic and cyclonic circulation in the middle troposphere. The red and blue shadings denote the warming and cooling in the lower troposphere.

a linear superposition of their individual effects, but rather as the result of the coupling between SSWs and Ural ridge anomalies. Nevertheless, given that there is a stationary wave source and climatological ridge over the Ural region during winter⁴⁷, it is expected that even in the absence of geopotential height anomalies in the Ural region prior to SSWs (i.e., when the Ural ridge is in its climatological mean state), similar mechanisms are at play: SSWs could modulate the propagation and migration of waves associated with the climatological Ural ridge. For example, previous studies only imposing a weak stratospheric polar vortex in model simulations without artificially altering Ural ridge anomalies have shown that waves propagating from the Ural region into the stratosphere are reduced⁵⁰, while the propagation below tropopause is enhanced, corresponding to the deepened trough over East Asia⁷⁰. Additionally, Zhang et al.⁵⁰ noted that the increase in blocking in response to weak stratospheric polar vortex exhibits zonally asymmetric patterns, primarily over the Atlantic sector, and those blockings tend to migrate from east to west, similar features as that shown in Figs. 3a–c and 6b. Further investigation is needed to clarify the relative contributions of the Ural ridge and stratospheric state to the surface responses to SSWs.

Methods

Identification of stratospheric events and datasets

In this study, daily temperature, winds, and geopotential height data on a $1^\circ \times 1^\circ$ grid from the ERA5 reanalysis dataset spanning from 1940–2020 are used, provided by the European Centre for Medium-Range Weather Forecasts (ECMWF)⁷¹. We note the results are similar to those obtained using reanalysis data spanning 1979–2020, when satellite observations became available (not shown). Additionally, datasets from 1979 to 2014 in historical experiments of 20 Coupled Model Intercomparison Project 6 (CMIP6) models⁷² are used, with most being high-top models (model lid above 1 hPa). These CMIP6 models include AWI-ESM-1-1-LR⁷³,

CanESM5⁷⁴, EC-Earth3⁷⁵, GFDL-CM4⁷⁶, GFDL-ESM4⁷⁷, GISS-E2-1-G⁷⁸, GISS-E2-2-G⁷⁹, HadGEM3-GC31-LR⁸⁰, INM-CM5-0⁸¹, IPSL-CM6A-LR⁸², IPSL-CM6A-LR-INCA⁸³, MIROC6⁸⁴, MPI-ESM-1-2-HAM⁸⁵, MPI-ESM1-2-HR⁸⁶, MPI-ESM1-2-LR⁸⁷, MRI-ESM2-0⁸⁸, CESM2-WACCM⁸⁹, CNRM-CM6-1⁹⁰, CNRM-ESM2-1⁹¹, UKESM1-0-LL⁹² (Table S1). Daily anomalies are calculated by removing the climatological seasonal cycle and linearly detrending in ERA5 and each individual CMIP6 ensemble member.

Following Charlton and Polvani⁹³, the onset date of SSWs is defined as the day when the daily zonal mean zonal wind at 10 hPa and 60°N reverses to easterly between November and March. To distinguish from final stratospheric warmings the wind must return to westerly for at least 20 consecutive days. Subsequently, the SSWs are categorized into two groups. If the area-averaged 500 hPa geopotential height anomalies over the Ural region (50°–80°N, 40°–80°E) from day –8 – –4 days relative to the SSW onset date are >0 gpm, the case is labeled as a strong Ural ridge SSW (SUR-SSWs), otherwise, it is considered a weak Ural ridge SSW (WUR-SSWs). The results are not very sensitive to the selected time and space ranges used for averaging the geopotential height over the Ural region. Using this definition, 29 SUR-SSWs and 22 WUR-SSWs are identified in ERA5, with their onset dates listed in Table S2. Additionally, it yields similar results if SUR-SSWs (WUR-SSWs) are selected based on the 850 hPa temperature anomaly over the BKS region (60°–80°N, 60°–80°E) from day –8 – –4 before SSW onset being greater or less than 0 K.

To understand the importance of the stratospheric state for the tropospheric evolution during SUR-SSWs and WUR-SSWs, these events are compared with strong polar vortex (SPV) events. SPV onset date is identified when the daily zonal mean zonal wind at 10 hPa and 60°N is >50 m/s, which leads to a comparable number of SPV events (56) to SSW events⁹⁴.

As the composite differences between the two types of SSW derived from reanalysis data may be influenced by internal variability, we conducted

three 115-member ensemble experiments (SUR-SSWs, WUR-SSWs and CLIMnudge) using the specified chemistry version of the Whole Atmosphere Community Climate Model (WACCM-SC)⁹⁵. The model's horizontal resolution is $1.9^\circ \times 2.5^\circ$, with 66 vertical levels extending from 1000 hPa to ~ 0.0006 hPa. Greenhouse gas emissions, radiatively active gas concentrations, solar radiation, sea ice concentration, and sea surface temperatures are prescribed to follow the same annual cycle. The ensemble runs are initiated from 115 different initial fields on January 1st, derived from a 125 year simulation with the same model without nudging. During the initial 32 days of SUR-SSWs and WUR-SSWs runs (corresponding to 1st January to February 1st of model time), temperatures and wind fields in the stratospheric polar region (north of 55°N and above 170 hPa) are nudged towards the same composite state observed from day -30 to day 1 of all SSWs in the period from 1980 to 2019. Meanwhile, temperature and wind fields in the tropospheric Ural region (ranging from 55°N to 80°N , 50°E to 90°E , and below 500 hPa) are nudged towards the composite state observed from day -30 to day 1 of SUR-SSWs (WUR-SSWs) for the SUR-SSWs (WUR-SSWs) run. For the CLIMnudge run, the temperature and wind fields in the stratospheric polar region and in the tropospheric Ural region during the initial 32 days are nudged towards the daily climatological state observed from 1st January to February 1st in the period from 1980 to 2019. After the 32 day nudging period of the three ensemble experiments, which corresponds to the period leading up to SSW onset, the experiments continue freely.

Dynamical diagnostics

To obtain Rossby wave phase speed, the daily wavenumber-zonal phase speed spectrum on each latitude circle is calculated using geopotential height within a 31 day sliding window centered on each day^{96,97}. The Rossby wave phase speed is defined as the spectral-weighted mean phase speed for wavenumbers $1 - 8$ ^{48,98,99}.

To diagnose the wave propagation environment, the daily wave refractive index squared n^2 is calculated as^{100,101}:

$$n^2(y, z) = \left(\frac{N^2}{f^2 \cos^2 \phi} \right) \left[\frac{\bar{q}_\phi}{\bar{u}} - \left(\frac{k}{a} \right)^2 - \left(\frac{f \cos \phi}{2NH} \right)^2 \right] \quad (1)$$

where a , H , k , \bar{q}_ϕ and \bar{u} represent the Earth's radius, scale height, zonal wave number ($k = 1$ for wavenumber one), meridional gradient of zonal mean quasi-geostrophic PV and zonal mean westerly, respectively. Waves tend to propagate in regions of positive n^2 and avoid negative values. To quantify the preferred direction of wave propagation, the daily negative frequency of n^2 is calculated as the fraction of negative n^2 values within the $50^\circ - 80^\circ\text{N}$ latitude band per day^{102,29}.

The daily propagation of planetary waves in vertical and zonal directions is calculated as¹⁰³:

$$(F_x, F_z) = p \cos \phi \left\{ \begin{array}{l} \frac{1}{2a^2 \cos^2 \phi} \left[\left(\frac{\partial \psi'}{\partial \lambda} \right)^2 - \psi' \frac{\partial^2 \psi'}{\partial \lambda^2} \right] \\ \frac{2\Omega^2 \sin^2 \phi}{N^2 a \cos \phi} \left(\frac{\partial \psi'}{\partial \lambda} \frac{\partial \psi'}{\partial z} - \psi' \frac{\partial^2 \psi'}{\partial \lambda \partial z} \right) \end{array} \right\} \quad (2)$$

where p represents the pressure divided by 1000 hPa, ϕ , λ , z denotes latitude, longitude and altitude, respectively. N^2 is the square of the buoyancy frequency, Ω and a denotes rotation speed and radius of the Earth, ψ' denotes the zonal deviation of the streamfunction.

Following the growth stage of baroclinic waves, Rossby Wave Breaking (RWB) occurs, characterized by the meridional overturning of PV on isentropic surfaces and the irreversible mixing of PV and heat¹⁰⁴. The RWB occurrence at each grid point is identified when the meridional PV gradient on the isentropic surface becomes negative¹⁰⁵. The daily RWB frequency is then calculated as the fraction of RWB occurrence within the $50^\circ - 80^\circ\text{N}$ latitude band per day.

Data availability

ERA5 datasets are available from <https://cds.climate.copernicus.eu/>. CMIP6 data are available from <https://esgf-node.llnl.gov/projects/esgf-llnl/>. The WACCM ensemble experiments that support the findings of this study are available upon reasonable request from the authors.

Code availability

All codes are available upon reasonable request from the authors.

Received: 3 April 2024; Accepted: 28 October 2024;

Published online: 17 November 2024

References

1. Plumb, R. A. & Semeniuk, K. Downward migration of extratropical zonal wind anomalies. *J. Geophys. Res. Atmos.* <https://doi.org/10.1029/2003GL017965> (2003).
2. Scott, R. K. & Polvani, L. M. Stratospheric control of upward wave flux near the tropopause. *Geophys. Res. Lett.* <https://doi.org/10.1029/2002JD002773> (2004).
3. Kolstad, E. W., Breiteig, T. & Scaife, A. A. The association between stratospheric weak polar vortex events and cold air outbreaks in the Northern Hemisphere. *Q J. R. Meteor. Soc.* **136**, 886–893 (2010).
4. Butler, A. H. et al. Defining sudden stratospheric warmings. *B Am. Meteorol. Soc.* **96**, 1913–1928 (2015).
5. Hall, R. J., Mitchell, D. M., Seviour, W. J. M., Wright, C. J. Tracking the stratosphere-to-surface impact of sudden stratospheric warmings. *J. Geophys. Res. Atmos.* **126**, e2020JD033881 (2021).
6. Baldwin, M. P. et al. Sudden stratospheric warmings. *Rev. Geophys.* **59**, e2020RG000708 (2021).
7. Ambaum, M. H. P. & Hoskins, B. J. The NAO troposphere–stratosphere connection. *J. Clim.* **15**, 1969–1978 (2002).
8. Baldwin, M. P. & Dunkerton, T. J. Propagation of the arctic oscillation from the stratosphere to the troposphere. *J. Geophys. Res.* **104**, 30937–30946 (1999).
9. Baldwin, M. P. et al. Stratospheric memory and skill of extended-range weather forecasts. *Science* **301**, 636–640 (2003).
10. Black, R. X. Stratospheric forcing of surface climate in the arctic oscillation. *J. Clim.* **15**, 268–277 (2002).
11. Black, R. X. & McDaniel, B. A. Diagnostic case studies of the northern annular mode. *J. Clim.* **17**, 3990–4004 (2004).
12. Charlton, A. J., O'Neill, A., Lahoz, W. A. & Massacand, A. C. Sensitivity of tropospheric forecasts to stratospheric initial conditions. *Q J. R. Meteor. Soc.* **130**, 1771–1792 (2004).
13. Hartley, D. E., Villarín, J. T., Black, R. X. & Davis, C. A. A new perspective on the dynamical link between the stratosphere and troposphere. *Nature* **391**, 471–474 (1998).
14. Haynes, P. H. & Shepherd, T. G. The importance of surface pressure changes in the response of the atmosphere to zonally-symmetric thermal and mechanical forcing. *Q J. R. Meteor. Soc.* **115**, 1181–1208 (1989).
15. Zhang, C. Y., Zhang, J. K., Xu, M., Zhao, S. Y. & Xia, X. F. Impacts of stratospheric polar vortex Shift on the East Asian trough. *J. Clim.* **35**, 5605–5621 (2022).
16. Kushner, P. J. & Polvani, L. M. Stratosphere-troposphere coupling in a relatively simple AGCM: The role of eddies. *J. Clim.* **17**, 629–639 (2004).
17. Limpasuvan, V. & Hartmann, D. L. Eddies and the annular modes of climate variability. *Geophys Res Lett.* **26**, 3133–3136 (1999).
18. Hitchcock, P. & Simpson, I. R. The downward influence of stratospheric sudden warmings. *J. Atmos. Sci.* **71**, 3856–3876 (2014).
19. Kodera, K., Mukougawa, H. & Fujii, A. Influence of the vertical and zonal propagation of stratospheric planetary waves on tropospheric blockings. *J. Geophys. Res.-Atmos.* **118**, 8333–8345 (2013).
20. Kodera, K., Mukougawa, H., Maury, P., Ueda, M. & Claud, C. Absorbing and reflecting sudden stratospheric warming events and

- their relationship with tropospheric circulation. *J. Geophys. Res. Atmos.* **121**, 80–94 (2016).
21. Liu, M. C., Hu, D. Z. & Guan, Z. Y. Modulation of a long-lasting extreme cold event in Siberia by a minor sudden stratospheric warming and the dynamical mechanism involved. *Clim. Dynam* **60**, 797–811 (2023).
 22. Matthias, V. & Kretschmer, M. The influence of stratospheric wave reflection on North American cold spell. *Mon. Weather Rev.* **148**, 1675–1690 (2020).
 23. Nath, D., Chen, W., Cai, Z. L., Pogoreltsev, A. I. & Wei, K. Dynamics of 2013 sudden stratospheric warming event and its impact on cold weather over Eurasia: role of planetary wave reflection. *Sci. Rep. UK* **6**, 24174 (2016).
 24. Davis, N. A., Richter, J. H., Glanville, A. A., Edwards, J. & LaJoie, E. Limited surface impacts of the January 2021 sudden stratospheric warming. *Nat. Commun.* **13**, 1136 (2022).
 25. Domeisen, D. I. V. et al. The role of the stratosphere in subseasonal to seasonal prediction: 2. predictability arising from stratosphere-troposphere coupling. *J. Geophys. Res. Atmos.* **125**, e2019JD030923 (2020).
 26. Rao, J. et al. Impact of the initial stratospheric polar vortex state on East Asian spring rainfall prediction in seasonal forecast models. *Clim. Dynam* **60**, 4111–4131 (2023).
 27. Maycock, A. C. & Hitchcock, P. Do split and displacement sudden stratospheric warmings have different annular mode signatures? *Geophys. Res. Lett.* **42**, 10943–10951 (2015).
 28. Rao, J., Garfinkel, C. I. & White, I. P. Predicting the downward and surface influence of the February 2018 and January 2019 sudden stratospheric warming events in subseasonal to seasonal (S2S) models. *J. Geophys. Res. Atmos.* **125**, e2019JD031919 (2020).
 29. Zhang, R. et al. The corresponding tropospheric environments during downward-extending and nondownward-extending events of stratospheric northern annular mode anomalies. *J. Clim.* **32**, 1857–1873 (2019).
 30. Karpechko, A. Y., Hitchcock, P., Peters, D. H. W. & Schneidereit, A. Predictability of downward propagation of major sudden stratospheric warmings. *Q. J. R. Meteor. Soc.* **143**, 1459–1470 (2017).
 31. Sigmund, M., Scinocca, J. F., Khari, V. V. & Shepherd, T. G. Enhanced seasonal forecast skill following stratospheric sudden warmings. *Nat. Geosci.* **6**, 98–102 (2013).
 32. Yang, P. K., Bao, M. & Ren, X. J. Influence of preconditioned stratospheric state on the surface response to displacement and split sudden stratospheric warmings. *Geophys. Res. Lett.* **50**, e2023GL103992 (2023).
 33. Yang, P. K., Bao, M., Ren, X. J. & Tan, X. The role of vortex preconditioning in influencing the occurrence of strong and weak sudden stratospheric warmings in ERA5 reanalysis. *J. Clim.* **36**, 1197–1212 (2023).
 34. Ma, J., Chen, W., Yang, R. W., Ma, T. J. & Shen, X. C. Downward propagation of the weak stratospheric polar vortex events: the role of the surface arctic oscillation and the quasi-biennial oscillation. *Clim. Dynam.* **42**, 4117–4131 (2024).
 35. White, I. et al. The downward influence of sudden stratospheric warmings: association with tropospheric precursors. *J. Clim.* **32**, 85–108 (2019).
 36. Jucker, M. Are sudden stratospheric warmings generic? insights from an idealized GCM. *J. Atmos. Sci.* **73**, 5061–5080 (2016).
 37. Mitchell, D. M., Gray, L. J., Anstey, J., Baldwin, M. P. & Charlton-Perez, A. J. The influence of stratospheric vortex displacements and splits on surface climate. *J. Clim.* **26**, 2668–2682 (2013).
 38. Lehtonen, I. & Karpechko, A. Y. Observed and modeled tropospheric cold anomalies associated with sudden stratospheric warmings. *J. Geophys. Res. Atmos.* **121**, 1591–1610 (2016).
 39. White, I. P., Garfinkel, C. I., Cohen, J., Jucker, M. & Rao, J. The impact of split and displacement sudden stratospheric warmings on the troposphere. *J. Geophys. Res. Atmos.* **126**, e2020JD033989 (2021).
 40. Zou, C. T., Zhang, R. N., Zhang, P. F., Wang, L. & Zhang, R. H. Contrasting physical mechanisms linking stratospheric polar vortex stretching events to cold Eurasia between autumn and late winter. *Clim. Dynam.* **62**, 2399–2417 (2023).
 41. Lu, Q. et al. The sudden stratospheric warming in January 2021. *Environ. Res. Lett.* **16**, 084029 (2021).
 42. Bao, M., Tan, X., Hartmann, D. L. & Ceppi, P. Classifying the tropospheric precursor patterns of sudden stratospheric warmings. *Geophys. Res. Lett.* **44**, 8011–8016 (2017).
 43. Cho, H. O., Kang, M. J., Son, S. W. The predictability of the 2021 SSW event controlled by the zonal-mean state in the upper troposphere and lower stratosphere. *J. Geophys. Res. Atmos.* **128**, e2023JD039559 (2023).
 44. Kolstad, E. W. & Charlton-Perez, A. J. Observed and simulated precursors of stratospheric polar vortex anomalies in the Northern Hemisphere. *Clim. Dynam* **37**, 1443–1456 (2011).
 45. Zhong, W. G., Wu, Z. W. Impact of stratospheric variability on subseasonal temperature reversals during late winter over the mid-high latitudes of East Asia. *Atmos. Res.* **297**, 107115 (2024).
 46. Martius, O., Polvani, L. M., Davies, H. C. Blocking precursors to stratospheric sudden warming events. *Geophys. Res. Lett.* <https://doi.org/10.1029/2009GL038776> (2009).
 47. Sun, J. & Tan, B. K. Mechanism of the wintertime Aleutian low-icelandic low seesaw. *Geophys. Res. Lett.* **40**, 4103–4108 (2013).
 48. Schutte, M. K., Domeisen, D. I. V. & Riboldi, J. Opposite spectral properties of Rossby waves during weak and strong stratospheric polar vortex events. *EGU Sphere* **2023**, 1–30 (2023).
 49. Chen, X. D., Luo, D. H., Wu, Y. T., Dunn-Sigouin, E. & Lu, J. Nonlinear response of atmospheric blocking to early winter Barents-kara seas warming: an idealized model study. *J. Clim.* **34**, 2367–2383 (2021).
 50. Zhang, C. et al. Impacts of stratospheric polar vortex changes on tropospheric blockings over the Atlantic region. *Clim. Dynam* **62**, 4829–4848 (2024).
 51. Woollings, T. et al. The role of Rossby waves in polar weather and climate. *Weather Clim. Dynam.* **4**, 61–80 (2023).
 52. Yang, G.-Y. & Hoskins, B. J. Propagation of Rossby waves of nonzero frequency. *J. Atmos. Sci.* **53**, 2365–2378 (1996).
 53. Weinberger, I., Garfinkel, C. I., Harnik, N. & Paldor, N. Transmission and reflection of upward-propagating Rossby waves in the lowermost stratosphere: importance of the tropopause inversion layer. *J. Atmos. Sci.* **79**, 3263–3274 (2022).
 54. Weinberger, I., Garfinkel, C. I., White, I. P. & Birner, T. The efficiency of upward wave propagation near the tropopause: importance of the form of the refractive index. *J. Atmos. Sci.* **78**, 2605–2617 (2021).
 55. Grise, K. M., Thompson, D. W. J. & Birner, T. A global survey of static stability in the stratosphere and upper troposphere. *J. Clim.* **23**, 2275–2292 (2010).
 56. White, I. P. et al. The generic nature of the tropospheric response to sudden stratospheric warmings. *J. Clim.* **33**, 5589–5610 (2020).
 57. Strong, C. & Magnusdottir, G. Tropospheric Rossby wave breaking and the NAO/NAM. *J. Atmos. Sci.* **65**, 2861–2876 (2008).
 58. Rupp, P. M., Birner, T. Tropospheric eddy feedback to different stratospheric conditions in idealised baroclinic life cycles. *Weather Clim. Dynam.* **2**, 111–128 (2020).
 59. Cheung, H. N., Zhou, W., Mok, H. Y. & Wu, M. C. Relationship between Ural-Siberian blocking and the East Asian winter monsoon in relation to the Arctic oscillation and the El Niño-southern oscillation. *J. Clim.* **25**, 4242–4257 (2012).
 60. Domeisen, D. I. V., Garfinkel, C. I. & Butler, A. H. The teleconnection of El Niño southern oscillation to the stratosphere. *Rev. Geophys* **57**, 47–45 (2019).
 61. Garfinkel, C. I. et al. Weakening of the teleconnection from El Niño-southern oscillation to the arctic stratosphere over the past few

- decades: what can be learned from subseasonal forecast models? *J. Geophys. Res. Atmos.* **124**, 7683–7696 (2019).
62. Luo, B., Luo, D., Dai, A., Simmonds, I. & Wu, L. The modulation of interdecadal pacific oscillation and Atlantic multidecadal oscillation on winter Eurasian cold anomaly via the Ural blocking change. *Clim. Dynam.* **59**, 127–150 (2021).
 63. Palmeiro, F. M., García-Serrano, J. R., Ruggieri, P., Batté L. & Gualdi S. On the influence of ENSO on sudden stratospheric warmings. *J. Geophys. Res. Atmos.* **128**, e2022JD037607 (2023).
 64. Luo, B. et al. Different influences of La Niña types on the winter sub-seasonal Eurasian cold anomalies linked to Ural blocking. *Atmos. Res.* **299**, 107172 (2023).
 65. Luo B., Luo D., Dai A., Simmonds I. & Wu L. A connection of winter Eurasian cold anomaly to the modulation of ural blocking by ENSO. *Geophys. Res. Lett.* **48**, e2021GL094304 (2021).
 66. Xu M. et al. Distinct tropospheric and stratospheric mechanisms linking historical barents-kara sea-ice loss and late winter Eurasian temperature variability. *Geophys. Res. Lett.* **48**, e2021GL095262 (2021).
 67. Zhang, P., Wu, Y., Chen, G. & Yu, Y. North American cold events following sudden stratospheric warming in the presence of low Barents-Kara sea sea ice. *Environ. Res. Lett.* **15**, 124017 2020
 68. Zhang, R., Screen, J. A. & Zhang, R. Arctic and Pacific Ocean conditions were favourable for cold extremes over Eurasia and North America during winter 2020/21. *B. Am. Meteorol. Soc.* **103**, E2285–E2301 (2022).
 69. Zou, C. & Zhang, R. Arctic sea ice loss modulates the surface impact of autumn stratospheric polar vortex stretching events. *Geophys. Res. Lett.* **51**, e2023GL107221 (2024).
 70. Zhang, J. et al. Impacts of stratospheric polar vortex changes on wintertime precipitation over the northern hemisphere. *Clim. Dynam.* **58**, 3155–3171 (2022).
 71. Hersbach, H. et al. The ERA5 global reanalysis. *Q. J. R. Meteor. Soc.* **146**, 1999–2049 (2020).
 72. Meinshausen, M. et al. Historical greenhouse gas concentrations for climate modelling (CMIP6). *Geosci. Model Dev.* **10**, 2057–2116 (2017).
 73. Danek, C. et al. AWI AWI-ESM1.1LR Model Output Prepared for CMIP6 CMIP Historical. <https://openpolar.no/Record/ftdatacite:10.22033%2Fesgf%2Fcmip6.9328> (2024).
 74. Swart, N. C. et al. IPCC DDC: CCCma CanESM5 Model Output Prepared for CMIP6 CMIP Historical. Version 20190530. <https://www.wdc-climate.de/ui/entry?acronym=C6CMCCCEhir10111Amprwgn90429> (2023).
 75. Consortium EC-E. IPCC DDC: EC-Earth-Consortium EC-Earth3 Model Output Prepared for CMIP6 CMIP Historical. <https://www.wdc-climate.de/ui/entry?acronym=C6CMEEE3hir12111Siscogn91018> (2023).
 76. Guo, H. et al. IPCC DDC: NOAA-GFDL GFDL-CM4 Model Output Historical. <https://www.wdc-climate.de/ui/entry?acronym=C6CMNGGFChir111AmcltUx80701> (2023).
 77. Krasting, J. P. et al. IPCC DDC: NOAA-GFDL GFDL-ESM4 Model Output Prepared for CMIP6 CMIP Historical. <https://www.wdc-climate.de/ui/entry?acronym=C6CMNGGFE> (2024).
 78. Studies NGIfS. IPCC DDC: NASA-GISS GISS-E2.1G Model Output Prepared for CMIP6 CMIP Historical. <https://www.wdc-climate.de/ui/cmip6?input=CMIP6.CMIP.NASA-GISS.GISS-E2-1-G.historical> (2019).
 79. Studies NGIfS. NASA-GISS GISS-E2-2-G Model Output Prepared for CMIP6 CMIP Historical. <https://www.wdc-climate.de/ui/cmip6?input=CMIP6.CMIP.NASA-GISS.GISS-E2-2-G.historical>(2023).
 80. Ridley, J., Menary, M., Kuhlbrodt, T. & Andrews, M., Andrews, T. IPCC DDC: MOHC HadGEM3-GC31-LL Model Output Prepared For CMIP6 CMIP Historical. <https://www.wdc-climate.de/ui/entry?acronym=C6CMMOHGL> (2024).
 81. Volodin, E. et al. IPCC DDC: INM INM-CM5-0 Model Output Prepared for CMIP6 CMIP Historical. <https://www.wdc-climate.de/ui/cmip6?input=CMIP6.CMIP.INM.INM-CM5-0.historical> (2023).
 82. Boucher, O. et al. IPCC DDC: IPSL IPSL-CM6A-LR Model Output Prepared for CMIP6 CMIP Historical. <https://www.wdc-climate.de/ui/entry?acronym=C6CMIPCLhi> (2023).
 83. Boucher, O. et al. IPSL IPSL-CM6A-LR-INCA Model Output Prepared for CMIP6 CMIP Historical. <https://www.wdc-climate.de/ui/cmip6?input=CMIP6.CMIP.IPSL.IPSL-CM6A-LR-INCA.historical> (2023).
 84. Tatebe, H. & Watanabe M. IPCC DDC: MIROC MIROC6 Model Output Prepared for CMIP6 CMIP Historical. <https://www.wdc-climate.de/ui/entry?acronym=C6CMMIMiHi> (2023).
 85. Neubauer, D. et al. IPCC DDC: HAMMOZ-Consortium MPI-ESM1.2-HAM Model Output Prepared for CMIP6 CMIP Historical. <https://www.wdc-climate.de/ui/entry?acronym=C6CMHCME1hir3111Amrsgn91218> (2023).
 86. Jungclaus, J. et al. MPI-M MPI-ESM1.2-HR model output prepared for CMIP6 CMIP historical. <https://www.wdc-climate.de/ui/cmip6?input=CMIP6.CMIP.MPI-M.MPI-ESM1-2-HR.historical> (2023).
 87. Wieners, K. -H. et al. MPI-M MPI-ESM1.2-LR Model Output Prepared for CMIP6 CMIP Historical. <https://www.wdc-climate.de/ui/cmip6?input=CMIP6.CMIP.MPI-M.MPI-ESM1-2-LR.historical> (2023).
 88. Yukimoto, S. et al. IPCC DDC: MRI MRI-ESM2.0 Model Output Prepared for CMIP6 CMIP Historical. <https://www.wdc-climate.de/ui/entry?acronym=C6CMMRME0hi> (2023).
 89. Danabasoglu, G. IPCC DDC: NCAR CESM2-WACCM Model Output Prepared for CMIP6 CMIP Historical. <https://www.wdc-climate.de/ui/entry?acronym=C6CMNRCESWahi> (2023).
 90. Voldoire, A. IPCC DDC: CMIP6 Simulations of the CNRM-CERFACS Based on CNRM-CM6-1 model for CMIP experiment historical. <https://www.wdc-climate.de/ui/entry?acronym=C6CMCECC1hi> (2023).
 91. Seferian, R. IPCC DDC: CNRM-CERFACS CNRM-ESM2-1 Model Output Prepared for CMIP6 CMIP Historical. <https://www.wdc-climate.de/ui/entry?acronym=C6CMCECE1hi> (2024).
 92. Tang, Y. et al. IPCC DDC: MOHC UKESM1.0-LL Model Output Prepared for CMIP6 CMIP Historical. <https://www.wdc-climate.de/ui/entry?acronym=C6CMMOU0hi> (2024).
 93. Charlton, A. J. & Polvani, L. M. A new look at stratospheric sudden warmings. Part I: climatology and modeling benchmarks. *J. Clim.* **20**, 449–469 (2007).
 94. Huang, J. & Hitchcock, P. Defining arctic stratospheric polar vortex intensification events. *J. Geophys. Res. Atmos.* **128**, e2023JD039373 (2023).
 95. Smith, K. L., Neely, R. R., Marsh, D. R. & Polvani, L. M. The specified chemistry whole atmosphere community climate model (SC-WACCM). *J. Adv. Mod. Earth Syst.* **6**, 883–901 (2014).
 96. Hayashi, Y. A generalized method of resolving transient disturbances into standing and traveling waves by space-time spectral analysis. *J. Atmos. Sci.* **36**, 1017–1029 (1979).
 97. Randel, W. J. & Held, I. M. Phase speed spectra of transient eddy fluxes and critical layer absorption. *J. Atmos. Sci.* **48**, 688–697 (1991).
 98. Domeisen, D. I. V., Martius, O. & Jiménez-Esteve, B. Rossby wave propagation into the northern hemisphere stratosphere: the role of zonal phase speed. *Geophys. Res. Lett.* **45**, 2064–2071 (2018).
 99. Riboldi, J., Lott, F., D'Andrea, F. & Rivière, G. On the linkage between Rossby wave phase speed, atmospheric blocking, and arctic amplification. *Geophys. Res. Lett.* **47**, e2020GL087796 (2020).
 100. Andrews, D. G., Holton, J. R. & Leovy, C. B. *Middle Atmosphere Dynamics* 1st edn, Vol. 40 (Academic Press Inc., 1987).
 101. Holton, J. R. & Mass, C. Stratospheric vacillation cycles. *J. Atmos. Sci.* **33**, 2218–2225 (1976).

102. Li, Q., Graf, H. F. & Giorgetta, M. A. Stationary planetary wave propagation in northern hemisphere winter—climatological analysis of the refractive index. *Atmos. Chem. Phys.* **7**, 183–200 (2007).
103. Plumb, R. A. On the 3-dimensional propagation of stationary waves. *J. Atmos. Sci.* **42**, 217–229 (1985).
104. Tamarin-Brodsky, T. & Harnik, N. The relation between Rossby wave-breaking events and low-level weather systems. *Weather Clim. Dynam.* **5**, 87–108 (2024).
105. Hitchman, M. H. & Huesmann, A. S. A seasonal climatology of Rossby wave breaking in the 320–2000 K layer. *J. Atmos. Sci.* **64**, 1922–1940 (2007).

Acknowledgements

This research is supported by the National Natural Science Foundation of China (42394120, 42075062 and 42130601). This research is also supported by the Fundamental Research Funds for the Central Universities (lzujbky-2023-it11 and lzujbky-2021-ey04). We thank the scientific teams at the European Centre for Medium-Range Weather Forecasts (ECMWF) for providing ERA5 data. We acknowledge the World Climate Research Programme to coordinate and promote CMIP6 through its Working Group on Coupled Modeling. We thank various climate modeling groups for producing and making available their model outputs. We appreciate the Earth System Grid Federation (ESGF) for archiving the data and providing public access and the multiple funding agencies that support CMIP6 and ESGF. We also appreciate the computing support provided by Supercomputing Center of Lanzhou University.

Author contributions

Chongyang Zhang and Jiankai Zhang conceptualized and designed the project. Chongyang Zhang conducted the model experiments and carried out the data analysis. Jiankai Zhang, Amanda C. Maycock and Wenshou Tian contributed to the interpretation of the results, offered valuable suggestions, and revised the manuscript. All authors participated in writing and reviewing the paper.

Competing interests

The authors declare no competing interests.

Additional information

Supplementary information The online version contains supplementary material available at <https://doi.org/10.1038/s41612-024-00826-8>.

Correspondence and requests for materials should be addressed to Jiankai Zhang.

Reprints and permissions information is available at <http://www.nature.com/reprints>

Publisher's note Springer Nature remains neutral with regard to jurisdictional claims in published maps and institutional affiliations.

Open Access This article is licensed under a Creative Commons Attribution-NonCommercial-NoDerivatives 4.0 International License, which permits any non-commercial use, sharing, distribution and reproduction in any medium or format, as long as you give appropriate credit to the original author(s) and the source, provide a link to the Creative Commons licence, and indicate if you modified the licensed material. You do not have permission under this licence to share adapted material derived from this article or parts of it. The images or other third party material in this article are included in the article's Creative Commons licence, unless indicated otherwise in a credit line to the material. If material is not included in the article's Creative Commons licence and your intended use is not permitted by statutory regulation or exceeds the permitted use, you will need to obtain permission directly from the copyright holder. To view a copy of this licence, visit <http://creativecommons.org/licenses/by-nc-nd/4.0/>.

© The Author(s) 2024